RSC Advances

PAPER

View Article Online
View Journal | View Issue

Cite this: *RSC Adv.*, 2017, **7**, 56365

Improvement in the hydrogen storage performance of the as-milled Sm–Mg alloys using MoS_2 nano-particle catalysts

Zeming Yuan,[ab] Wei Zhang,[ab] Peilong Zhang,[c] Yanghuan Zhang, *[ab] Wengang Bu,[a] Shihai Guo[a] and Dongliang Zhao[a]

Received 12th September 2017
Accepted 22nd November 2017

DOI: 10.1039/c7ra10160k

rsc.li/rsc-advances

The effects of the addition of MoS_2 catalyst on the microstructure and hydrogen storage behavior of the as-milled Sm_5Mg_{41} alloys were investigated in this study. The Sm_5Mg_{41} + *x* wt% MoS_2 (*x* = 0, 5, and 10) alloys were prepared by milling MoS_2 powders (particle size ≤ 40 nm) and the mechanically ground as-cast Sm_5Mg_{41} alloy powders (particle size ≤ 75 μm) in an argon atmosphere for 5 h. The results demonstrate that the as-milled alloys are composed of Sm_5Mg_{41} and $SmMg_3$ phases and milling refines the crystal grains. The MgH_2 and Sm_3H_7 phases appear after hydrogenation, while the Mg and Sm_3H_7 phases are formed after dehydrogenation. MoS_2 nano-particles are embedded in the alloy surface, which is nanostructured with some crystal defects, such as dislocations, grain boundaries, and twins. These microstructures are advantageous in reducing the total potential barrier that the hydrogen absorption or desorption reaction must overcome, thus improving the hydrogen storage kinetics of the alloys. The dehydriding activation energies of the alloys are 122.28, 68.25, and 59.91 kJ mol^{-1} H_2 for *x* = 0, 5, and 10, respectively. The catalyzed alloys begin to release hydrogen at ~241.9 °C, which is 26.4 °C lower than the temperature required for non-catalyzed alloys. The hydrogenation enthalpies of the alloys are −81.72, −78.31, and −78.18 kJ mol^{-1} H_2 for *x* = 0, 5, and 10, respectively. Therefore, the addition of a MoS_2 catalyst significantly improves the hydrogen storage kinetics of Mg-based alloys.

Introduction

Hydrogen has extensive applications, including those in aviation, aerospace, metallurgy, and petrochemical industries. It would be successfully applied in commercial vehicles as one of the clean energy resources. The state-of-the-art sustainable H_2 production technologies have developed rapidly and H_2 fuel has widespread applications.[1–9] However, there are some bottlenecks in achieving the practical, efficient, safe, and cheap hydrogen storage systems.

Magnesium-based alloys are one of the most promising hydrogen storage alloys and have been studied extensively because of their high hydrogen storage capacity and low-cost.[10,11] However, they face some disadvantages in terms of their high dehydrogenation temperatures, slow dehydrogenation kinetics, and high reactivity with air and oxygen.[12,13] The key focus of the current research on such materials is on lowering their dehydrogenation temperature, improving their dehydrogenation kinetics, and prolonging their life cycle. Alloying, nanocrystallization, and catalyst addition are some of the helpful methods for obtaining the low-cost hydrogen storage materials with favorable thermodynamics and kinetics.[14,15]

Most of the current studies on the magnesium-based alloys for hydrogen storage focus on two main mechanisms for the dehydrogenation of MgH_2. The first mechanism is a "nucleation and growth" model of Mg in bulky particles.[16] Mg nucleates inside MgH_2 (including a spot of residual Mg) and grows with the diffusion of the H atoms. H_2 is synthesized when the H atoms diffuse to the surface of MgH_2, which indicates the end of the decomposition of MgH_2. The second model follows a "shrinking core" mechanism,[17] in which Mg nucleates initially on the surfaces of the MgH_2 nano-particles and then grows into the core of the material. Based on the diffusion of the H atoms through the newly formed Mg layer and the formation of the H_2 molecules, the decomposition of MgH_2 is accomplished. In both models, the diffusion rate of the H atoms is the controlling parameter. The diffusion rate of the H atoms in Mg (4×10^{-13}) is almost three orders of magnitude higher than that in MgH_2 (1.5×10^{-16}).[18,19] Thus, microstructure nanocrystallization is an effective tool to enhance the kinetics of dehydrogenation. Au *et al.*[20] fabricated MgH_2 nano-particles using carbon aerogels of large surface areas with pore sizes of 6–20 nm and demonstrated hydrogen release at 140 °C. This temperature is much

[a]*Department of Functional Material Research, Central Iron and Steel Research Institute, Beijing 100081, China. E-mail: zhangyh59@sina.com*

[b]*Key Laboratory of Integrated Exploitation of Baiyun Obo Multi-Metal Resources, Inner Mongolia University of Science and Technology, Baotou 014010, China*

[c]*Whole Win (Beijing) Materials Sci. & Tech. Co., Ltd., Beijing, China*

lower than that of other Mg-based hydrogen storage alloys. Moreover, this hydrogen storage material reached 80% of the maximum absorption capacity in just 15 min at 300 °C.

Using catalysts/additives to destabilize hydrides of high hydrogen storage density, *e.g.*, MgH_2 with 7.6 wt% H and a desorption temperature as high as 300–400 °C, is one of the most important strategies to improve the thermodynamics and kinetics of the hydrogen storage materials.[21–23] Cui *et al.*[24] pointed out that the Ti-based multivalent catalysts can improve the kinetics of the hydrogen storage materials. During the hydrogenation process, a diatomic Ti ion donates an electron to the hydrogen atom on the Mg surface and converts it into a hydrogen ion, while converting itself into a trivalent Ti ion. The hydrogen ion unites with a Mg atom and forms a weak Mg–H bond, resulting in a reduction in the energy barrier for hydrogenation and dehydrogenation. Lin *et al.*[25] reported a symbiotic $CeH_{2.73}/CeO_2$ catalyst to enhance the hydrogen storage capacity of MgH_2 and demonstrated that a spontaneous hydrogen release effect in the interface region of the symbiotic $CeO_2/CeH_{2.73}$ nano-particle played a role as an efficient "hydrogen pump". Shahi *et al.*[26] milled an intermetallic hydride, $ZrFe_2H_x$, with MgH_2 to synthesize the MgH_2–$ZrFe_2H_x$ nano-composites and found that $ZrFe_2H_x$ led to a decrease in the dehydrogenation temperature from 410 °C to 290 °C. Furthermore, it significantly improved the hydrogenation kinetics, as observed by the lowered activation energy of ~61 kJ mol^{-1} H_2. El-Eskandarany *et al.*[27] used the reactive ball milling (RBM) method to prepare $MgH_2/5Ni/5Nb_2O_5$ nanocomposite powders, which exhibited an excellent hydriding/dehydriding performance, as evidenced by the short time required to absorb (41 s) and desorb (121 s) 5 wt% H_2 at 250 °C. Although numerous new achievements have been reported, further efforts are urgently necessary to enhance the hydrogen storage performance of the Mg-based alloys.

To design a hydrogen storage material with the fast kinetics and a low desorption temperature, the investigations on the effects of the addition of Mo-containing catalysts to MgH_2 have been initiated.[28,29] It has also been reported that the catalysis of the S ions can improve the hydrogen storage kinetics of MgH_2.[29] In our previous study, we showed that an activated Sm–Mg alloy,[30,31] containing rare earth (RE) hydride nano-particles and high-density boundaries, can act as a potential Mg-based hydride. The hydrogen storage kinetics of the alloy can be enhanced because the nano-particles exert a catalytic action and the high-density boundaries can provide a number of channels for hydrogen diffusion. Therefore, the effects of adding MoS_2 nano-particle catalysts[32–35] on the microstructure and gaseous hydrogen storage behavior of the as-cast Sm_5Mg_{41} alloys are studied in the current investigation.

Experimental

The as-cast Sm_5Mg_{41} alloys composed of the major phase Sm_5Mg_{41} (93.367 wt%) and the secondary phase $SmMg_3$ (6.633 wt%) were manufactured according to the procedure reported in our previous work.[30] The MoS_2-catalyzed Sm_5Mg_{41} alloys were prepared by milling MoS_2 nano-particles (particle size ≤ 40 nm, Beijing Dk nano S&T Ltd.) along with the mechanically ground as-cast alloy powders (particle size ≤ 75 μm) at weight fractions of 0%, 5%, and 10% in an argon atmosphere for 5 h. The weight ratio of the powder mixture to Cr–Ni stainless steel balls was 1 : 40 and each tank revolved around its own axis at a constant speed of 350 rpm. In fact, the mass of the precursor was 5.00 g in every tank, but only 4.55 g can be collected as the final product because the material was stuck on the balls and the inner wall of the tank. The elemental compositions of the milled powders were analyzed by inductively coupled plasma atomic emission spectrometry (ICP-AES). The phase compositions and microstructures of the alloys were characterized using an X-ray diffractometer (XRD) and a field emission transmission electron microscope (FETEM, Tecnai G2 F30, operated at 200 kV) equipped with an energy dispersive X-ray spectrometer (EDS) and a selected area electron diffractometer (SAED). The sample (0.5 g) was loaded into a cylindrical reactor for analyzing the pressure–composition isotherms (P–C-I) and the hydrogen absorption/desorption kinetics, which were measured by a PCT Automatic Measuring System (PCT-4SDWIN, Suzuki Shokan Co. Ltd.) in a furnace controlled at an accuracy of ±1 °C. Before measurement, each sample was subjected to five abovementioned hydriding/dehydriding cycles with the hydrogenation reaction occurring at 340 °C and 3 MPa and the dehydrogenation reaction occurring at 340 °C and 1×10^{-4} MPa. The P–C-I curves were recorded at 320, 340, 360, and 380 °C in a hydrogen pressure range from 0.05 MPa to 3 MPa. The hydrogen absorption analysis was conducted at a pressure of 3 MPa and the temperatures of 270, 300, 360, and 380 °C, while the desorption analysis was conducted at a pressure of 1×10^{-4} MPa and the temperatures of 300, 320, 340, and 360 °C. The non-isothermal dehydrogenation performance of the alloys was investigated by thermogravimetry (TG, TGA, Q600) at a heating rate of 5 °C min^{-1} in an argon atmosphere (99.99% purity, 36 mL min^{-1} flow rate).

Results and discussion

Composition, structure, and hydriding/dehydriding mechanism

The actual compositions of the $Sm_5Mg_{41} + x$ wt% MoS_2 ($x = 0$, 5, and 10) alloys were measured by ICP-AES to be $Sm_5Mg_{41} + x$ wt% MoS_2 ($x = 0$, 5, and 10), indicating that there was no contamination by Fe or other impurities; the compositions of the samples are listed in Table 1.

The XRD patterns of the milled $Sm_5Mg_{41} + x$ wt% MoS_2 ($x =$ 0, 5, and 10) alloys before and after the hydrogen absorption

Table 1 The actual compositions of the $Sm_5Mg_{41} + x$ wt% MoS_2 ($x = 0$, 5, 10) alloys measured by ICP

$Sm_5Mg_{41} +$ x wt% MoS_2	Sm (wt%)	Mg (wt%)	Mo (wt%)	Fe (wt%)
$x = 0$	42.99 ± 0.21	57.02 ± 0.29	0.00	0
$x = 5$	40.84 ± 0.20	54.16 ± 0.27	3.00 ± 0.02	0
$x = 10$	38.69 ± 0.19	51.31 ± 0.26	5.99 ± 0.03	0

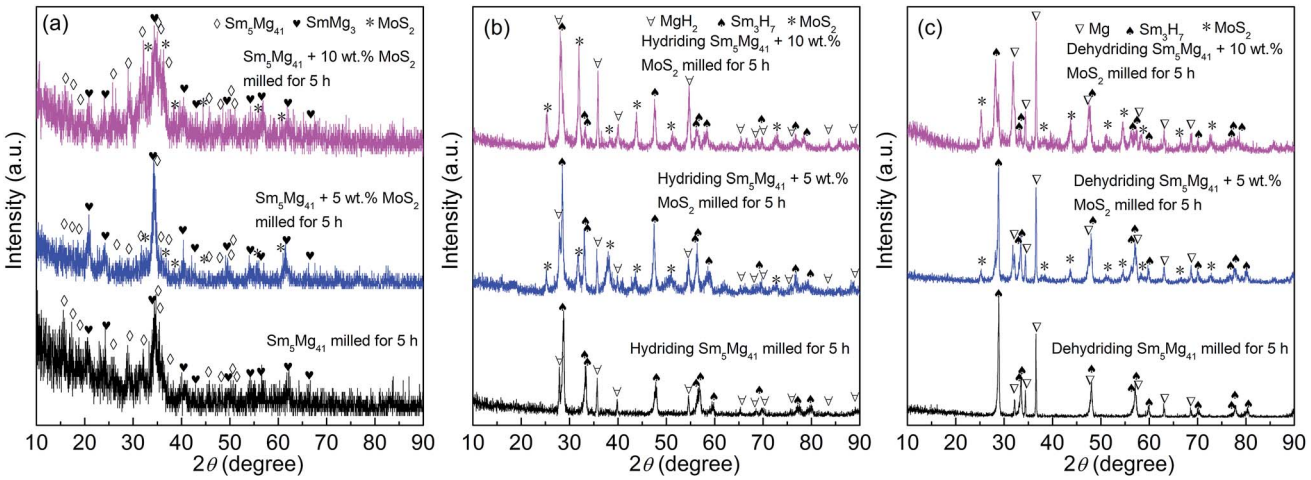

Fig. 1 XRD patterns of the Sm_5Mg_{41} + x wt% MoS_2 (x = 0, 5, and 10) alloys milled for 5 h: (a) before hydriding; (b) after hydriding; (c) after dehydriding.

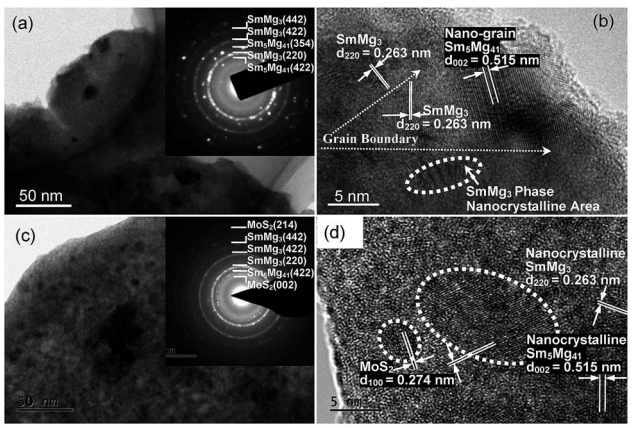

Fig. 2 SAED and TEM micrographs of the non-catalyzed (a and b) and the 5 wt% MoS_2 catalyzed (c and d) Sm_5Mg_{41} alloys before the hydrogen absorption.

and desorption are depicted in Fig. 1. ICDD identification of the XRD patterns reveals that the milled alloys contain Sm_5Mg_{41} as the major phase and $SmMg_3$ as the secondary phase before the hydrogen absorption. It is worth noting that milling causes a significant broadening of the diffraction peaks, implying the grain refining by ball milling. Moreover, this broadening phenomenon is reinforced by the addition of a MoS_2 catalyst, which always exists in all of the catalyzed alloys due to its higher stability, suggesting that the addition of the MoS_2 catalyst facilitates the grain refinement and the production of a nanocrystalline microstructure. It can be observed from Fig. 1(b) that three phases, MoS_2, Sm_3H_7, and MgH_2, are present in the hydrogenated catalyzed alloys and there are evident crystallization reactions taking place, as reflected by the sharp peaks. The MoS_2, Sm_3H_7, and Mg phases can be also found in the dehydrogenated catalyzed alloys (see Fig. 1(c)), suggesting the high thermal stabilities for the Sm_3H_7 hydride and the MoS_2 catalyst phases during the hydriding/dehydriding cycle. Based

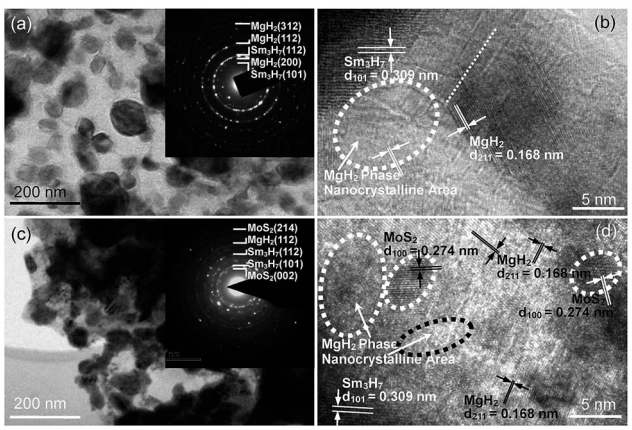

Fig. 3 SAED and TEM micrographs of the non-catalyzed (a and b) and the 5 wt% MoS_2 catalyzed (c and d) Sm_5Mg_{41} alloys after the hydrogen absorption.

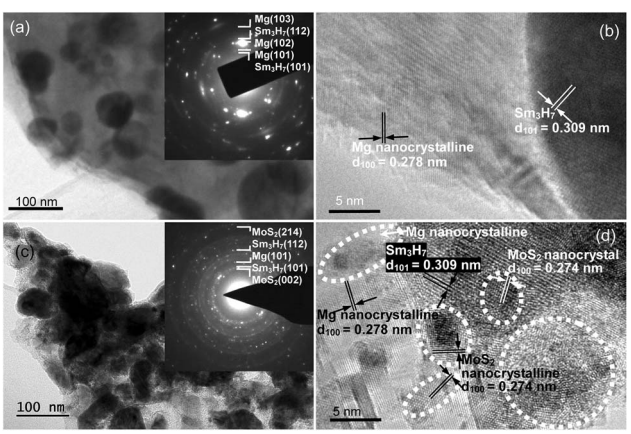

Fig. 4 SAED and TEM micrographs of the non-catalyzed (a and b) and the 5 wt% MoS_2 catalyzed (c and d) Sm_5Mg_{41} alloys after the hydrogen desorption.

on the XRD results, a hydride formation pathway is suggested: $Sm_5Mg_{41} + SmMg_3 + H_2 \rightarrow Sm_3H_7 + MgH_2 \leftrightarrow Sm_3H_7 + Mg + H_2$.

Fig. 2 shows the bright field TEM images, SAED rings, and HRTEM images of the milled (5 h) $Sm_5Mg_{41} + x$ wt% MoS_2 (x = 0 and 5) alloys before the hydrogen absorption. Based on the crystallographic electron diffraction calibration results (see the insets in Fig. 2(a) and (c)), it could be confirmed that the alloys contain the $SmMg_3$ and Sm_5Mg_{41} phases with an added MoS_2 phase in the catalyzed alloys. These results are consistent with the XRD observations. A focus zone was randomly chosen to determine the microstructure of the alloys as shown in Fig. 2(b) and (d). As observed in the HRTEM images, the internal microstructure of the alloys contains the Sm_5Mg_{41} nanocrystals with a 0.515 nm interplanar spacing in the (002) direction, the $SmMg_3$ nanocrystals with a 0.262 nm interplanar spacing in the (220) direction, and numerous structural defects, including nanocrystallites, lattice dislocations, grain boundaries, and micro-twins. The MoS_2 nanocrystals with an interplanar spacing of 0.277 nm in the (200) direction were observed to be embedded in the surfaces of the catalyzed alloys.

Fig. 3 and 4 depict the bright field TEM images, SAED rings, and HRTEM images of the fully hydrogenated $Sm_5Mg_{41} + x$ wt% MoS_2 (x = 0 and 5) alloys before and after the hydrogen desorption, respectively. The Sm_3H_7 nano-particles surrounded by a MgH_2 matrix-phase can be clearly observed in the hydrogenated alloy. This observation is also supported by the SAED pattern shown in the inset in Fig. 3(a). Moreover, a MoS_2 phase is present in the catalyzed alloys (see Fig. 3(c)). A MgH_2

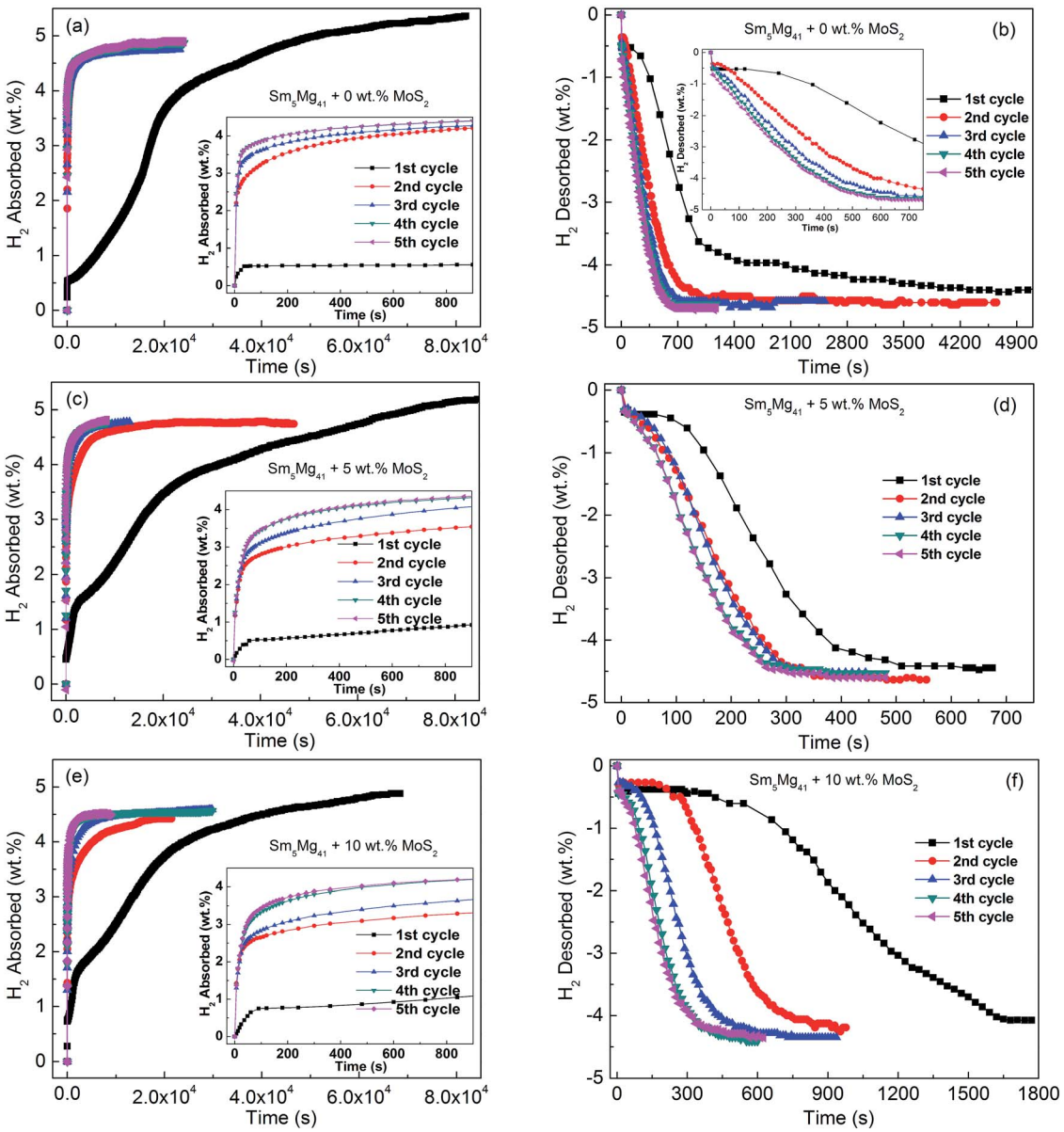

Fig. 5 The isothermal hydrogen absorption and desorption curves of the $Sm_5Mg_{41} + x$ wt% MoS_2 (x = 0, 5, and 10) alloys in the cycle activation with the hydrogenation reaction at 340 °C and 3 MPa and the hydrogenation reaction at 340 °C and 1×10^{-4} MPa: (a) and (b) $x = 0$; (c) and (d) $x = 5$; and (e) and (f) $x = 10$.

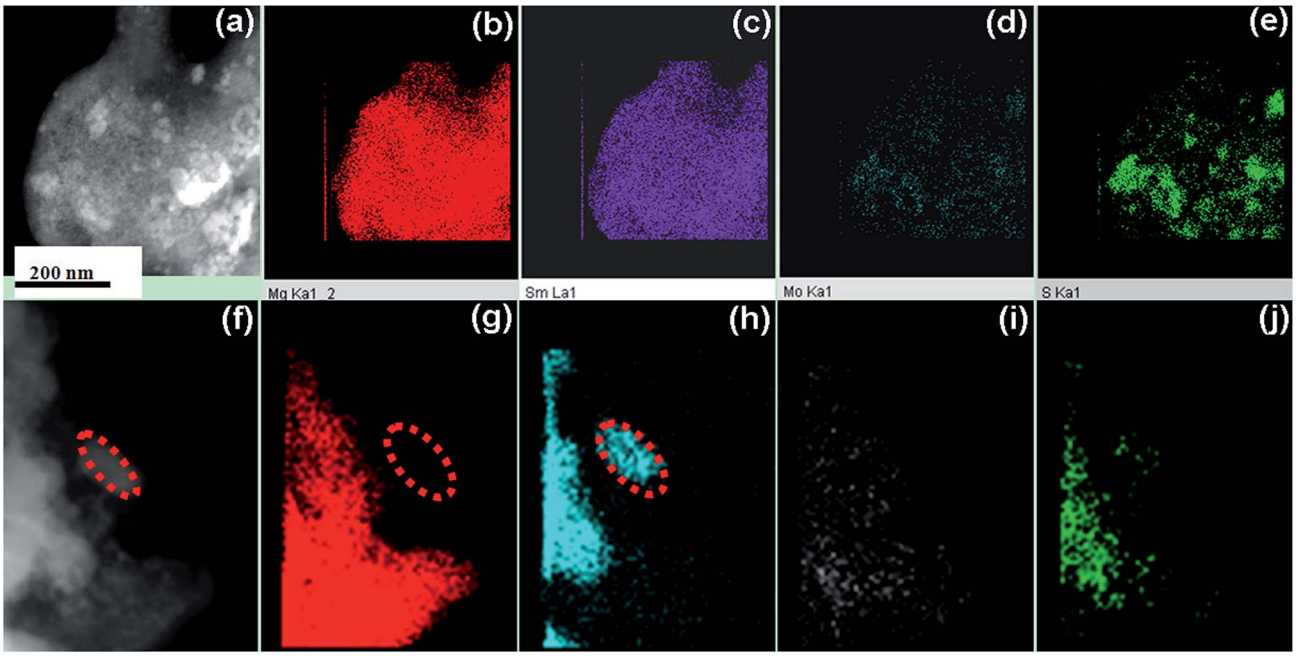

Fig. 6 FETEM micrographs and EDS mapping of the 5 wt% MoS_2 catalyzed Sm_5Mg_{41} alloys before the hydrogen absorption (a–e) and the hydrogenated sample after the hydrogen absorption (f–j).

polycrystalline phase and some crystal defects such as dislocations, grain boundaries, and twins are clearly observed in the dehydrogenated alloys (see Fig. 3(b) and (d)). It can be seen from Fig. 4(b) and (d) that after dehydrogenation, the Sm_3H_7 particles exhibit an almost integrated structure with an interplanar spacing of 0.309 nm in the (211) direction, while being surrounded by a Mg phase, in which some crystal defects including lattice dislocations, grain boundaries, and nanocrystals can be clearly observed. Moreover, the MoS_2 nanocrystals embedded in the alloy surface can be clearly observed in the catalyzed alloys both before and after the hydrogen desorption.

Fig. 5 displays the isothermal hydrogenation and dehydrogenation curves of the Sm_5Mg_{41} + x wt% MoS_2 ($x = 0$, 5, and 10) alloys activated by five hydriding and dehydriding cycles with the hydrogenation reaction occurring at 340 °C and 3 MPa and the dehydrogenation reaction occurring at 340 °C and 1×10^{-4} MPa. It can be observed that after more than 5 hydriding/dehydriding cycles, the hydrogen absorption/desorption capacities are about 5.01 wt%, 4.81 wt%, and 4.59 wt% for $x = 0$, 5, and 10, respectively, and the curves remain almost unchanged with a further increase in the number of cycles. Notably, the initial maximum hydrogen capacities are 5.36 wt%, 5.21 wt%, and 4.88 wt% for $x = 0$, 5, and 10, respectively, which are higher than their reversible hydrogen absorption/desorption capacities, indicating that there exist undecomposed hydrides of Sm_3H_7 in the Sm_5Mg_{41} + x wt% MoS_2 ($x = 0$, 5, and 10) alloys during the hydrogen absorption/desorption process. Moreover, the shortest initial hydriding time is exhibited by the $x = 5$ alloy, indicating that the addition of MoS_2 markedly improves the initial hydriding progress of the alloy. However, the improvement is hindered when an excess catalyst is added because the surface of the alloy is covered by the catalyst. However, the addition of MoS_2 by milling significantly enhances the reversible hydrogen absorption/desorption rate of the alloy after the initial hydriding cycle. Specifically, the time for complete hydrogen desorption of the Sm_5Mg_{41} alloy at 340 °C is reduced from 4900 s to 400 s when MoS_2 is added as a catalyst.

The FETEM analysis was conducted to investigate the changes in the microstructure and the phase distribution of the 5 wt% MoS_2-catalyzed Sm_5Mg_{41} alloy before and after the hydrogen absorption. Fig. 6 shows the bright field FETEM images and the EDS mapping results, in which the red, purple,

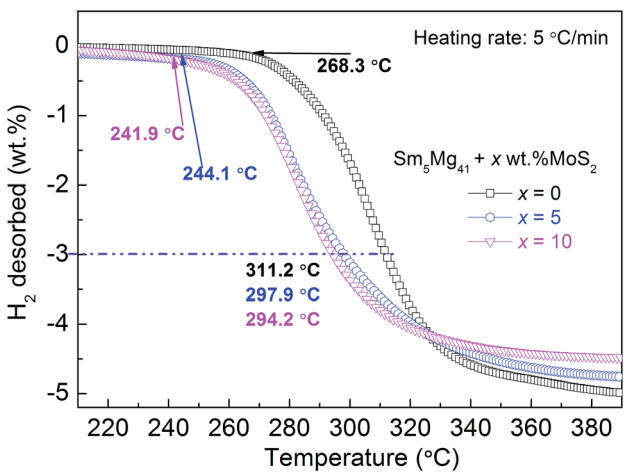

Fig. 7 Temperature programmed desorption curve of the Sm_5Mg_{41} + x wt% MoS_2 ($x = 0$, 5, and 10) alloys after the hydrogen absorption at a heating rate of 5 °C min^{-1}.

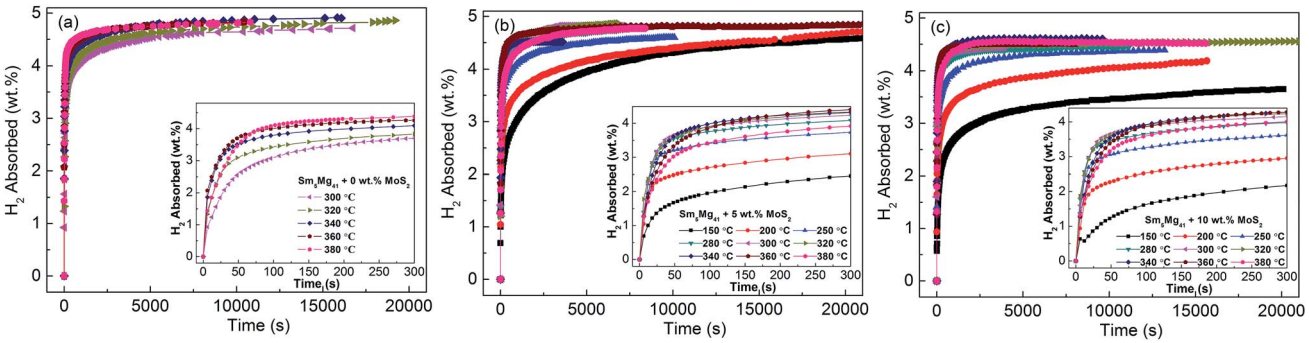

Fig. 8 Isothermal hydrogenation kinetic curves of the Sm_5Mg_{41} + *x* wt% MoS_2 (*x* = 0, 5, 10) alloys at different temperatures: (a) *x* = 0; (b) *x* = 5; and (c) *x* = 10.

cyan, and green points represent the distributions of Mg, Sm, Mo, and S elements, respectively. As shown in Fig. 6(b) and (c), the Mg and Sm elements have nearly the same distribution in the alloy before the hydrogen absorption. However, the Sm element separates from the Mg element after the hydrogen absorption (see Fig. 6(g) and (h)), indicating the atomic migration of Sm and Mg in the Mg-based Sm_5Mg_{41} alloy during the first hydrogen absorption process. Moreover, Mo and S always exhibit nearly the same distribution in the alloy both before and after the hydrogen absorption. This finding shows that the first hydriding cycle induces an irreversible decomposition of the alloy with the formation of a Mg hydride and the corresponding Sm hydride according to the following mechanism: Sm_5Mg_{41} + $SmMg_3$ + H_2 → Sm_3H_7 + MgH_2. The nucleation and growth mechanism of the formed Sm_3H_7–MgH_2 composites can be described as follows. The Mg-based Sm_5Mg_{41} alloy initially transforms into Sm_3H_7 and Mg and then into the Sm_3H_7–MgH_2 composites during the hydrogenation process.[30] Moreover, the MoS_2 phase is stable.

Hydrogen desorption temperature

To investigate the relationship between the H-desorption temperature and the hydrogen desorption capacity, the temperature programmed desorption curves of the hydrogenated Sm_5Mg_{41} + *x* wt% MoS_2 (*x* = 0, 5, and 10) alloys were constructed at a heating rate of 5 °C min^{-1} (Fig. 7). It can be observed that three non-isothermal dehydrogenation curves are similar in shape, but the initial temperatures of the hydrogen release are different, *i.e.*, 268.3, 244.1, and 241.9 °C for *x* = 0, 5, and 10, respectively. There is a visible decrease of 16.4 °C in the initial dehydriding temperature. Moreover, the dehydriding temperatures of the alloys are 311.2, 297.9, and 294.2 °C for *x* = 0, 5, and 10, respectively, corresponding to 3 wt% of the hydrogen desorption capacity, while that of pure MgH_2 is 428 °C.[21] From the above description, it can be inferred that the dehydriding temperature decreased significantly due to the catalytic action of MoS_2 and Sm_3H_7 nano-particles.

Hydrogen storage kinetics

In order to understand the influence of the addition of MoS_2 catalyst on the hydrogenation kinetics of the Sm_5Mg_{41} alloys, the isothermal hydrogenation kinetic curves of the alloys were constructed at different temperatures (Fig. 8). It is evident that the catalyst can significantly decrease the temperature of the hydrogen absorption. The absorption temperature of the catalyzed Sm_5Mg_{41} alloys with 5 wt% and 10 wt% MoS_2 dramatically decreases to 150 °C. Moreover, the hydriding capacities of the experimental samples can reach the values of 3.0 wt% at 200 °C within 300 s. However, the maximum hydrogen absorption capacities are 5.01, 4.87, and 4.60 wt% for the non-catalyzed alloy, 5 wt%-added alloy, and 10 wt%-added alloy, respectively. The reduction in the maximum capacity is attributed to

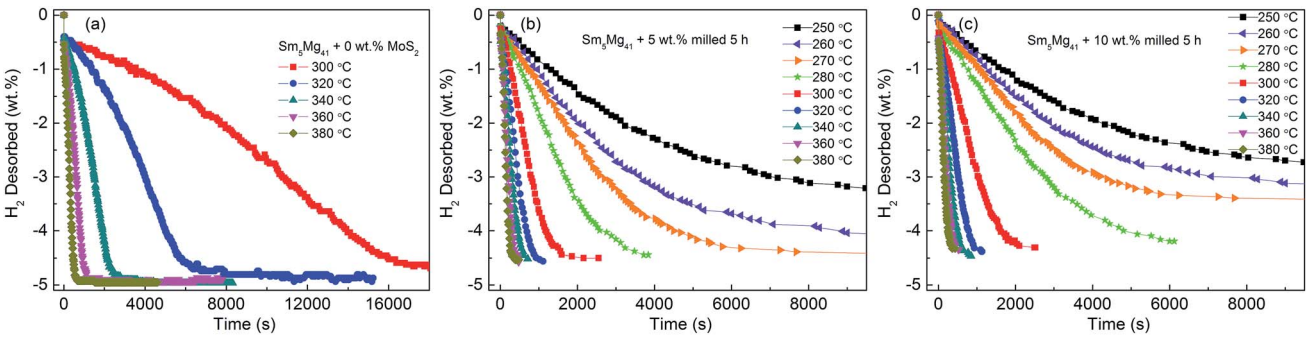

Fig. 9 Isothermal dehydrogenation kinetic curves of the Sm_5Mg_{41} + *x* wt% MoS_2 (*x* = 0, 5, and 10) alloys at different temperatures: (a) *x* = 0; (b) *x* = 5; and (c) *x* = 10.

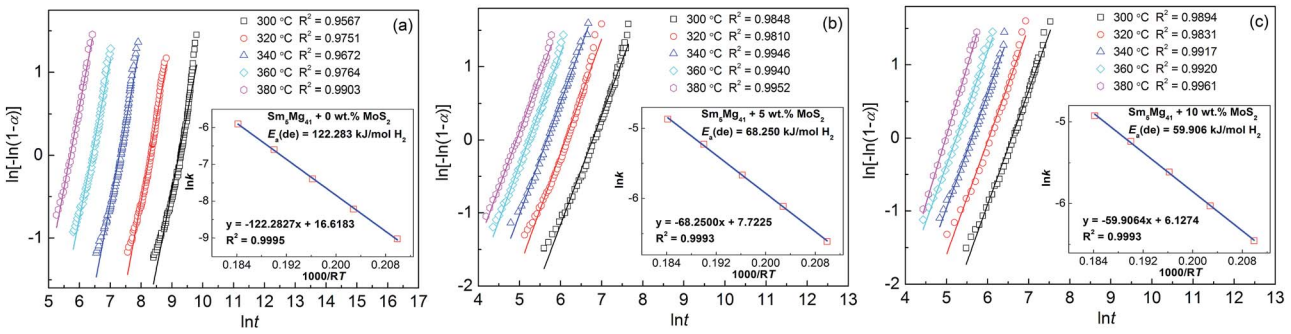

Fig. 10 JMA plots and Arrhenius plots for the dehydrogenation of the Sm_5Mg_{41} + x wt% MoS_2 (x = 0, 5, and 10) alloys: (a) x = 0; (b) x = 5; and (c) x = 10.

the inability of the catalyst to react with H_2 and produce the hydrides. Thus, it can be deduced that the catalyst can markedly enhance the hydriding properties. The catalytic action can be explained as follows. The catalyst enhances the rate of diffusion of H_2 and decreases the dissociation energy of H_2 into the H atoms on the surfaces of the alloys.

Fig. 9 shows the hydrogen desorption curves of the as-milled Sm_5Mg_{41} alloys with different MoS_2 loadings at different temperatures. The dehydrogenation capacities of the alloys decrease with an increase in the MoS_2 weight fraction because of its dead-weight. In other words, the maximum dehydrogenation capacities of the Sm_5Mg_{41} + x wt% MoS_2 (x = 0, 5, and 10) alloys at 360 °C are 4.88 wt%, 4.57 wt%, and 4.35 wt%, respectively, for x = 0, 5, and 10. These values are lower than their hydrogenation capacity values because the stored hydrogen cannot be desorbed fully in a closed test system. The times to desorb 3.5 wt% hydrogen at 300, 320, 340, 360, and 380 °C are 12 180, 4530, 1704, 702, and 352 s, respectively, in the case of the non-catalyzed Sm_5Mg_{41} alloy, 970, 552, 362, 244, and 184 s, respectively, in the case of the 5 wt% MoS_2 added Sm_5Mg_{41} alloy, and 1272, 621, 386, 261, and 199 s in the case of the 10 wt% MoS_2 added Sm_5Mg_{41} alloy. It can be observed from the comparison that the dehydriding rates decrease with a decrease in the temperature. Adding 5 wt% MoS_2 markedly improves the dehydrogenation kinetics of the Sm_5Mg_{41} alloy, but the improvement is hindered when an excess catalyst is added because of its dead-weight.

Hydrogen desorption activation energy is an important factor in describing the dehydrogenation kinetics of an alloy.[36] In this study, we chose the Arrhenius method to describe the effect of the MoS_2 addition on the dehydrogenation process. The dehydrogenation kinetics is primarily determined by the energy barrier, which needs to be overcome before MgH_2 can release H_2. The activation energy is defined as the total energy overcome during the dehydrogenation process. In the current study, the dehydrogenation process of Sm_5Mg_{41} follows a nucleation and growth process. The Johnson–Mehl–Avrami (JMA) model is used to simulate this process as follows:

$$\ln[-\ln(1-\alpha)] = \eta \ln k + \eta \ln t \quad (1)$$

where α is the phase fraction transformed at time t, which can be identified using a normalized hydrogen wt% (range from 0 to 1), η is the Avrami exponent, and k is an effective kinetic parameter. Using the logarithmic form of eqn (1), the JMA plots of $\ln[-\ln(1-\alpha)]$ *vs.* $\ln t$ can be drawn at the temperatures of 300, 320, 340, 360, and 380 °C at different MoS_2 contents, as shown in Fig. 10. The fitting lines of the JMA plots are almost linear, which indicates that the dehydrogenation reaction exhibits an instantaneous nucleation followed by an interface-controlled three-dimensional growth process. The slope and intercept of the JMA plots represent the values of η and $\eta \ln k$, respectively, from which the value of the rate constant k could be deduced. Using the Arrhenius method, the dehydrogenation activation energy E_a(de) can be calculated as follows:

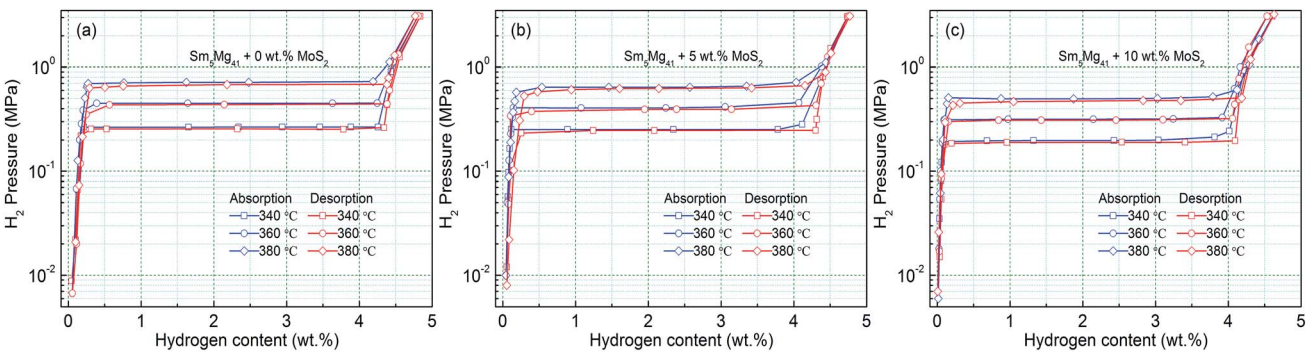

Fig. 11 P–C-I curves of the Sm_5Mg_{41} + x wt% MoS_2 (x = 0, 5, and 10) alloys measured at different temperatures: (a) x = 0; (b) x = 5; and (c) x = 10.

Table 2 Plateau pressures from the P–C-I curves at different temperatures and the calculated enthalpy and entropy for the hydrogen absorption and desorption process of the MoS_2 catalyzed Sm_5Mg_{41} alloys

As-milled 5 h Sm_5Mg_{41} alloys		Plateau pressure (MPa) 340 °C	360 °C	380 °C	Thermodynamic parameters ΔH (kJ mol^{-1})	ΔS (J K^{-1} mol^{-1})
Non-added	Absorption	0.266	0.451	0.716	−82.3868	−161.6095
	Desorption	0.255	0.438	0.684	82.0241	160.7176
Added 5 wt% MoS_2	Absorption	0.252	0.407	0.645	−78.1844	−135.1105
	Desorption	0.246	0.394	0.625	77.5607	133.8804
Added 10 wt% MoS_2	Absorption	0.197	0.317	0.497	−76.9900	−131.1250
	Desorption	0.190	0.309	0.479	76.9502	130.7887

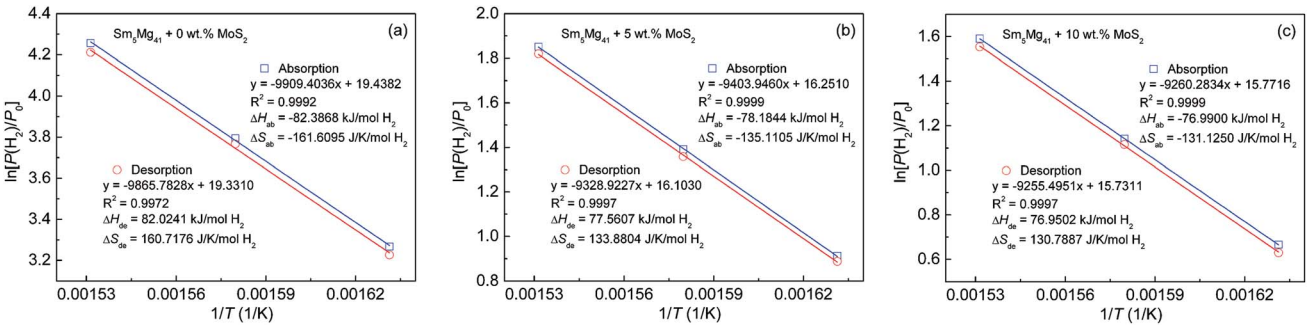

Fig. 12 Van't Hoff plots of the Sm_5Mg_{41} + x wt% MoS_2 (x = 0, 5, and 10) alloys measured at different temperatures: (a) x = 0; (b) x = 5; and (c) x = 10.

$$k = A \exp[-E_a(\mathrm{de})/RT] \quad (2)$$

where k is an effective kinetic parameter, as defined previously, A is a temperature independent coefficient, R is the universal gas constant (8.3145 J mol^{-1} K^{-1}), and T is the absolute temperature. Using the logarithmic transform of eqn (2), the Arrhenius plots of ln k *vs.* 1/T can be drawn as shown in the inset in Fig. 10. The fitting lines of all of the Arrhenius plots are almost linear. From the slopes of the fitting lines, the activation energies of the Sm_5Mg_{41} alloys are calculated to be 122.28, 68.25, and 59.91 kJ mol^{-1} H_2 for x = 0, 5, and 10, respectively, which indicates that the activation energies of the Sm_5Mg_{41} alloys decreased with an increase in the MoS_2 content. The nano-MoS_2 used as the catalysts markedly reduces the energy barrier and lowers the driving forces required for nucleation during the dehydrogenation reaction. In addition, the E_a(de) value of the as-milled Sm_5Mg_{41} alloy is much lower than that of pure milled MgH_2 (158.5 kJ mol^{-1} H_2),[37] suggesting that Sm_3H_7 can catalyze the desorption reaction of MgH_2, and the similar results have been demonstrated in the Sm_5Mg_{41} alloys.[30]

Hydrogen storage thermodynamics

In order to analyze the influence of the catalyst on the hydrogen storage thermodynamics of the Sm_5Mg_{41} + x wt% MoS_2 (x = 0, 5, and 10) alloys, the P–C-I curves were constructed at different temperatures. Fig. 11 shows that each curve has only one flat hydrogen equilibrium plateau. The thermodynamic data obtained from the P–C-I measurements are listed in Table 2. It can be found that the absorption/desorption pressure plateaus reduce with an increase in the MoS_2 content, which attributes to Mo that can facilitate the dissociation of hydrogen.[38]

According to the absorption/desorption pressure plateaus, the thermodynamic parameters, *viz.*, enthalpy change (ΔH) and entropy change (ΔS), can be estimated from the Van't Hoff equation[30] as shown below:

$$\ln[P(\mathrm{H_2})/P_0] = \Delta H/(RT) - \Delta S/R \quad (3)$$

where P_0 = 1 atm, and R and $P(H_2)$ refer to the gas constant and the equilibrium plateau pressure, respectively. The Van't Hoff curves ($\ln[P(H_2)/P_0]$ *vs.* 1/T) are illustrated in Fig. 12. According to the slopes and intercepts of the fitting lines obtained from the experimental data, the thermodynamic parameters can be calculated (Table 2). The changes in the hydrogenation enthalpies (ΔH_{ab}) are 82.39, 78.18, and 76.99 kJ mol^{-1} H_2 for x = 0, 5, and 10, respectively, while the corresponding changes in the dehydrogenation enthalpies (ΔH_{de}) are −82.02, −77.56, and −76.95 kJ mol^{-1} H_2. However, the ΔH_{de} value of the experimental alloys is very close to that of pure Mg, namely, −76 to −78 kJ mol^{-1},[39,40] which suggests that the addition of a MoS_2 catalyst could not change the thermodynamic properties in terms of the hydrogen storage in the Mg-based alloys.

Conclusions

(1) The alloys are composed of the nanocrystal phases of Sm_5Mg_{41}, $SmMg_3$, and MoS_2. Mechanical milling and catalyst

doping lead to a reduction in the particle sizes. These particles can store a strain energy, which contributes to an improvement in the hydrogen storage kinetics. The MoS_2 phase is stable during the absorption/desorption cycling process. The MgH_2 and Sm_3H_7 phases are formed after the hydrogen absorption, while the Mg and Sm_3H_7 phases are generated after the hydrogen desorption. The hydriding/dehydriding reaction mechanism is as follows: $Sm_5Mg_{41} + SmMg_3 + H_2 \rightarrow Sm_3H_7 + MgH_2 \leftrightarrow Sm_3H_7 + Mg + H_2$.

(2) The activation energies of dehydrogenation are estimated to be 122.283, 68.250, and 59.906 kJ mol^{-1} H_2 at the MoS_2 catalyst contents of 0, 5, and 10 wt%, respectively, which suggests that the nano-MoS_2 reduces the energy barrier and lowers the driving forces required for nucleation during the dehydrogenation reaction.

(3) The catalyzed alloys begin to release hydrogen at ~241.9 °C, which is ~26.4 °C lower than that of the non-catalyzed alloy. The hydrogenation enthalpy of the 10 wt% MoS_2-catalyzed alloy is determined to be ~76.99 kJ mol^{-1} H_2, which is very close to that of pure Mg, indicating that catalyst addition could not alter the thermodynamic properties in terms of the hydrogen storage in the Mg-based alloys.

Conflicts of interest

There are no conflicts to declare.

Acknowledgements

This work is financially supported by the National Natural Science Foundations of China (51761032, 51471054 and 51371094) and Natural Science Foundation of Inner Mongolia, China (2015MS0558).

References

1 W. Li, X. F. Gao, D. H. Xiong, F. Wei, W. G. Song, J. Y. Xu and L. F. Liu, *Adv. Energy Mater.*, 2017, **7**, 1602579.
2 W. Li, X. F. Gao, D. H. Xiong, F. Xia, J. Liu, W. G. Song, J. Y. Xu, S. M. Thalluri, M. F. Cerqueira, X. L. Fu and L. F. Liu, *Chem. Sci.*, 2017, **8**, 2952–2958.
3 W. Li, D. H. Xiong, X. F. Gao, W. G. Song, F. Xia and L. F. Liu, *Catal. Today*, 2017, **287**, 122–129.
4 W. Li, X. F. Gao, X. G. Wang, D. H. Xiong, P. P. Huang, W. G. Song, X. Q. Bao and L. F. Liu, *J. Power Sources*, 2016, **330**, 156–166.
5 W. Li, X. G. Wang, D. H. Xiong and L. F. Liu, *Int. J. Hydrogen Energy*, 2016, **41**, 9344–9354.
6 X. G. Wang, W. Li, D. H. Xiong, D. Y. Petrovykh and L. F. Liu, *Adv. Funct. Mater.*, 2016, **26**, 4067–4077.
7 C. Y. Cao, C. Q. Chen, W. Li, W. G. Song and W. Ca, *ChemSusChem*, 2010, **3**, 1241–1244.
8 F. Z. Song, W. Li and Y. J. Sun, *Inorganics*, 2017, **5**, 40.
9 X. G. Wang, W. Li, D. H. Xiong and L. F. Liu, *J. Mater. Chem. A*, 2016, **4**, 5639–5646.
10 D. L. Zhao and Y. H. Zhang, *Rare Met.*, 2014, **33**, 499–510.
11 M. Anik, F. Karanfil and N. Küçükdeveci, *Int. J. Hydrogen Energy*, 2012, **37**, 299–308.
12 M. S. L. Hudson, K. Takahashi, A. Ramesh, S. Awasthi, A. K. Ghosh, P. Ravindran and O. N. Srivastava, *Catal. Sci. Technol.*, 2016, **6**, 261–268.
13 M. Lototskyy, J. M. Sibanyoni, R. V. Denys, M. Williams, B. G. Pollet and V. A. Yartys, *Carbon*, 2013, **57**, 146–160.
14 N. V. Mushnikov, A. E. Ermakov, M. A. Uimin, V. S. Gaviko, P. B. Terent'ev, A. V. Skripov, A. P. Tankeev, A. V. Solonin and A. L. Buzlukov, *Phys. Met. Metallogr.*, 2006, **102**, 421–431.
15 M. Tanniru, H. Y. Tien and F. Ebrahimi, *Scr. Mater.*, 2010, **63**, 58–60.
16 M. Zhu, Y. Gao, X. Z. Che, Y. Q. Yang and C. Y. Chung, *J. Alloys Compd.*, 2002, **330**, 708–713.
17 K. Nogita, Q. T. Xuan, T. Yamamoto, E. Tanaka, S. D. Mcdonald, C. M. Gourlay, K. Yasuda and S. Matsumura, *Sci. Rep.*, 2015, **5**, 8450.
18 J. Qu, Y. Wang, L. Xie, J. Zheng, Y. Liu and X. Li, *J. Power Sources*, 2009, **186**, 515–520.
19 P. Spatz, H. A. Aebischer, A. Krozer and L. Schlapbach, *Z. Phys. Chem.*, 1993, **181**, 393–397.
20 Y. S. Au, M. K. Obbink, S. Srinivasan, P. C. M. M. Magusin, K. P. De Jong and P. E. De Jongh, *Adv. Funct. Mater.*, 2014, **24**, 3604–3611.
21 Rafi-ud-din, X. Qu, P. Li, Z. Lin, M. Ahmad, M. Z. Iqbal, M. Y. Rafique and M. H. Farooq, *RSC Adv.*, 2012, **2**, 4891–4903.
22 N. Juahir, N. S. Mustafa, A. M. Sinin and M. Ismail, *RSC Adv.*, 2015, **5**, 60983–60989.
23 H. Liu, C. Wu, H. Zhou, T. Chen, Y. Liu, X. Wang, D. Zhaohui, H. Ge, S. Li and M. Yan, *RSC Adv.*, 2015, **5**, 22091–22096.
24 J. Cui, H. Wang, J. Liu, L. Ouyang, Q. Zhang, D. Sun, X. Yao and M. Zhu, *J. Mater. Chem. A*, 2013, **1**, 5603–5611.
25 H. J. Lin, J. J. Tang, Q. Yu, H. Wang, L. Z. Ouyang, Y. J. Zhao, J. W. Liu, W. H. Wang and M. Zhu, *Nano Energy*, 2014, **9**, 80–87.
26 R. R. Shahi, A. Bhatanagar, S. K. Pandey, V. Shukla, T. P. Yadav, M. A. Shaz and O. N. Srivastava, *Int. J. Hydrogen Energy*, 2015, **40**, 11506–11513.
27 M. S. El-Eskandarany, H. S. AlMatrouk and E. Shaban, *Mater. Today*, 2016, **3**, 2735–2743.
28 M. Tian and C. Shang, *J. Chem. Sci. Tech.*, 2012, **1**, 54–59.
29 Y. Jia, S. Han, W. Zhang, X. Zhao, P. Sun, Y. Liu, H. Shi and J. Wang, *Int. J. Hydrogen Energy*, 2013, **38**, 2352–2356.
30 Z. Yuan, T. Yang, W. Bu, H. Shang, Y. Qi and Y. Zhang, *Int. J. Hydrogen Energy*, 2016, **41**, 5994–6003.
31 Y. Zhang, W. Zhang, Z. M. Yuan, W. Bu, Y. Qi and S. Guo, *Int. J. Hydrogen Energy*, 2017, **42**, 17157–17166.
32 X. D. Li, G. X. Wu, J. W. Chen, M. C. Li, W. Li, T. Y. Wang, B. Jiang, Y. He and L. Q. Mai, *Appl. Surf. Sci.*, 2017, **392**, 297–304.
33 W. Li, D. H. Chen, F. Xia, J. Z. Y. Tan, J. Song, W. G. Song and R. A. Caruso, *Chem. Commun.*, 2016, **52**, 4481–4484.
34 X. D. Li, W. Li, M. C. Li, P. Cui, D. H. Chen, T. Gengenbach, L. H. Chu, H. Y. Liu and G. S. Song, *J. Mater. Chem. A*, 2015, **3**, 2762–2769.

35 D. H. Xiong, Q. Q. Zhang, W. Li, J. J. Li, X. L. Fu, M. F. Cerqueira, P. Alpuim and L. F. Liu, *Nanoscale*, 2017, **9**, 2711–2717.
36 M. Pourabdoli, S. Raygan, H. Abdizadeh and D. Uner, *Int. J. Hydrogen Energy*, 2013, **38**, 11910–11919.
37 J. Mao, Z. Guo, X. Yu, H. Liu, Z. Wu and J. Ni, *Int. J. Hydrogen Energy*, 2010, **35**, 4569–4575.
38 S. Srivastava and K. Panwar, *Mater. Renew. Sustain. Energy*, 2015, **4**, 19–29.
39 J. X. Zou, H. Guo, X. Q. Zeng, S. Zhou, X. Chen and W. J. Ding, *Int. J. Hydrogen Energy*, 2013, **38**, 10912–10918.
40 Y. Zhang, M. Ji, Z. Yuan, W. Bu, Y. Qi and S. Guo, *RSC Adv.*, 2017, 7, 37689–37698.